Non-Hermitian spectrum and multistability in exciton-polariton condensates

Zi-Fa Yu,[1,2,3] Ju-Kui Xue,[3] Lin Zhuang,[1,*] Jinkui Zhao ◉,[2,4,*] and Wu-Ming Liu ◉[2,4]

[1]*State Key Laboratory of Optoelectronic Materials and Technologies, School of Physics, Sun Yat-Sen University, Guangzhou 510275, China*
[2]*Beijing National Laboratory for Condensed Matter Physics, Institute of Physics, Chinese Academy of Sciences, Beijing 100190, China*
[3]*Key Laboratory of Atomic & Molecular Physics and Functional Materials of Gansu Province,*
College of Physics and Electronic Engineering, Northwest Normal University, Lanzhou 730070, China
[4]*Songshan Lake Materials Laboratory, Dongguan 523808, China*

We investigate non-Hermitian spectrum and multistability of exciton-polariton condensates excited by a non-resonant pump. An increase in pumping power moves the system away from non-Hermitian spectrum degeneracy toward bifurcation through an exceptional point, which induces a transition from monostability to multistability. The spectrum can be used as a universal method for detecting this transition. In the region of multistability, the system contains one steady and two metastable states. The analyses of stability show that metastable states maintain a finite lifetime and eventually evolve into steady states, which are induced by non-Hermitian skin effects. We also discover a steady state with multipeak soliton for attractive polariton-polariton interaction, which is different from general single-peak soliton for repulsive interaction. Our results open up exciting possibilities for controlling non-Hermitian quantum multistable states, which may be useful for designing polariton-based devices exploiting optical multistability.

I. INTRODUCTION

Multistability, where multiple stable states simultaneously present for a given set of parameters, is a fascinating phenomenon in various physical systems, such as semiconductor microcavities [1], atomic Bose-Einstein condensates [2,3], magnetic materials [4], and optical systems [5]. It can be used for applications in digital optical devices [6], integrated optical circuits [7], and all-optical switches [8–10]. Such multistability-based devices have the advantages of robustness, simplicity, high-speed switching [10], and low-power operation [11].

Recently, multistability has aroused enormous attention in exciton-polariton Bose-Einstein condensates (EPCs) [12–25] owing to their room-temperature condensation [26–30], quantum nonequilibrium, and non-Hermitian nature [31–34]. They can be directly imaged in momentum and real space [35,36] as well as highly controlled via suitably manipulating both optical pump and quantum-well microcavities [37] in experiments. In such a system, various multistable phenomena have been discovered [20–25] such as vortex multistability, spin multistability, spatial multistability, and parity bifurcation transition of multistable states. Generally, the generation of EPC multistability requires polariton-polariton interactions which can induce Kerr nonlinearity [14–16]. Moreover, the overall competition among cavity anisotropy, spinor interactions, and excitation laser polarization dictates spin multistability [38]. The mechanism of spatial multistability is associated with repulsive cross-interactions among different polariton modes [23]. The driven-dissipative character of nonlinear polariton fluids can give rise to multistability of the flat band nonlinear domains [39].

As a natural non-Hermitian system [40–50], the spectral structures of EPCs are modified by non-Hermiticity, which affects the steady state, localization, nonlinearity, transportation, and dynamics of the system [45–50]. However, it is still not clear whether multistability can be related to non-Hermiticity. If so, can multistability be explained by the corresponding non-Hermitian spectrum? This would lie at the heart of this multistable phenomena since spectrum degeneracy can reveal novel transition, while the corresponding non-Hermitian eigenenergy is related to the stability of multistable states and influences relevant dynamical properties [35]. For a Hermitian system, corresponding eigenstates are always nondegenerate when energy spectrum degenerates. However, for a non-Hermitian system, energy spectrum degeneracy is accompanied by the coalescence of eigenstates. In a non-Hermitian spectrum, there are exceptional points [51–53] where multiple eigenstates collapse and corresponding eigenmodes coalesce into one. These exceptional points can cause a range of peculiar phenomena, such as unidirectional transmission of signals [54], anomalous absorption of lasing [55], and chiral modes [56]. Certainly they can also affect the transition of multistability. Therefore, can a non-Hermitian spectrum provide a universal method for detecting the transition from monostability to multistability?

In this paper, we reveal the formation mechanism of multistable states associated with the non-Hermitian spectrum bifurcation in EPCs excited by a nonresonant Gaussian pump [see Fig. 1(a)]. In experiments [26–30,35,36], generally quantum wells (QWs) are GaAs thin layers with the order of 10 nm thickness, and distributed Bragg reflectors consist of

---

*Corresponding authors: stszhl@mail.sysu.edu.cn; jkzhao@iphy.ac.cn
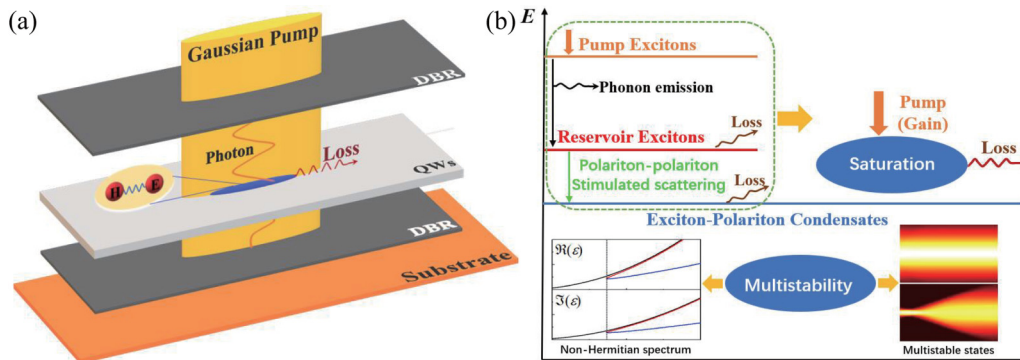
FIG. 1. (a) Schematic diagram of semiconductor microcavity device supporting exciton-polariton condensates (EPCs) in quasi-one-dimensional semiconductor microwire. The device is comprised of QWs placed between two distributed Bragg reflectors (DBRs). Polaritons are excited by a nonresonant Gaussian pump beams incident from above. (b) Schematic representation of the mechanism for generating EPCs.

multiple pairs of alternated AlAs and GaAs layers. EPCs have a typical lifetime on the order of 100 ps and condensation temperature on the order of 10 K in GaAs and CdTe semiconductors. The pump produces a reservoir of high-energy excitons which scatter continuously into lower energy polaritons. When scattering amplification overcomes losses, condensates are formed. In adiabatic approximations, the reservoir can be regarded as static and it moderates condensate densities. The system can be modeled by considering effective gain (pump), loss, and saturation [see Fig. 1(b)]. Our results indicate that increasing pumping power moves the system away from the non-Hermitian spectrum degeneracy toward bifurcation through an exceptional point, which induces the multistability of EPCs. The exceptional point of spectrum is exactly the transition point of multistability. By constructing a diagram of multistability and the dynamical evolution of multistable states, we are able to control the multistability, and discover a steady state with multipeak solitons for attractive EPCs, which is different from sing-peak soliton for repulsive EPCs.

II. EXCITON-POLARITON CONDENSATE SYSTEM

Motivated by relevant experiments of EPCs [26–30,57], we consider a nonequilibrium EPC system excited by a nonresonant one-dimensional continuous-wave pump with a Gaussian profile (see Fig. 1). Under the mean-field approach, EPCs can be described by a dimensionless open-dissipative Gross-Pitaevskii equation [31,32,58–63]:

$$i\frac{\partial \psi}{\partial t} = \left[-\frac{1}{2}\nabla^2 + g|\psi|^2 + \frac{i}{2}\left(P(x) - \gamma - \eta|\psi|^2\right)\right]\psi. \quad (1)$$

Here the physical variables are rescaled as $\psi \sim l^{-1/2}\psi$, $t \sim \omega^{-1}t$, and $x \sim lx$ with condensate characteristic length $l = \sqrt{\hbar/(m\omega)}$ and characteristic frequency ω; m is the polariton effective mass; g is the dimensionless polariton-polariton interaction constant. $P(x)$ is a spatially modulated Gaussian pump with power P_0 and width w, i.e., $P(x) = P_0 e^{-x^2/w^2}$; γ is the polariton loss rate; η refers to the gain saturation. For a nonresonantly pumped system, gain saturation is necessarily present. Without gain saturation, the condensate grows indefinitely when the pump exceeds loss and vanishes when the pump falls short of loss [58]. The steady state described by

this saturation is similar to the one described by considering a static reservoir of noncondensed polaritons [60]. Equation (1) can be derived by adopting a so-called adiabatic approximation to eliminate the reservoir adiabatically [58–60], i.e., the density of reservoir n_R satisfies $\partial n_R/\partial t = 0$.

To obtain a solution for steady states and dynamical evolutions, we use the variational method for dissipative systems [64,65]. A natural variational ansatz is the Gaussian trial distribution,

$$\psi(x,t) = \left(\frac{n}{\sqrt{\pi}R}\right)^{1/2} \exp\left[-\frac{(x-\xi)^2}{2R^2} + ik(x-\xi) + \frac{i\delta}{2}(x-\xi)^2 + i\phi\right], \quad (2)$$

which denotes that EPCs have a Gaussian distribution with the center mass position $\xi(t)$, momentum $k(t)$, size $R(t)$, related variation rate of width $\delta(t)$, phase $\phi(t)$, and the number $n(t)$ (i.e., $n = \int |\psi|^2 dx$) at a given time t. After variational analyses, we obtain the dynamics of related variational parameters $q_i(t)$ ($q_i = \{\xi, k, R, \delta, n, \phi\}$), equilibrium states (i.e., $q_i(t) \equiv \bar{q}_i$), and non-Hermitian energies (for details, see Appendix A).

EPCs are formed when the pumping power is larger than the threshold $P_0^{th} = \sqrt{\gamma/2}(1 + \sqrt{1 + 2\gamma w^2}/w)$, which is independent of the polariton-polariton interaction and the gain saturation. It is reduced by the pumping size and promoted by the loss rate. For a homogeneous pump (i.e., $w \to \infty$), $P_0^{th} = \gamma$. A nonresonant Gaussian pump can result in damped dipolar oscillation and create the self-localization of EPCs (Appendix C).

III. NON-HERMITIAN SPECTRUM

Figure 2 demonstrates the non-Hermitian spectrum of EPCs for different pumping powers and polariton-polariton interactions. There is one exceptional point in the non-Hermitian spectrum for different pumping powers at $P_0 = P_{0c}$ as shown in Figs. 2(a1)–2(a3). For weak pumping powers, i.e., $P_0^{th} < P_0 < P_{0c}$, the non-Hermitian spectrum is degenerate with only one energy, which corresponds to a steady state. For strong pumping powers, i.e., $P_0 > P_{0c}$, increasing pumping power moves the system away from the spectral degeneracy, and spectrum bifurcation occurs. In this case, there are three
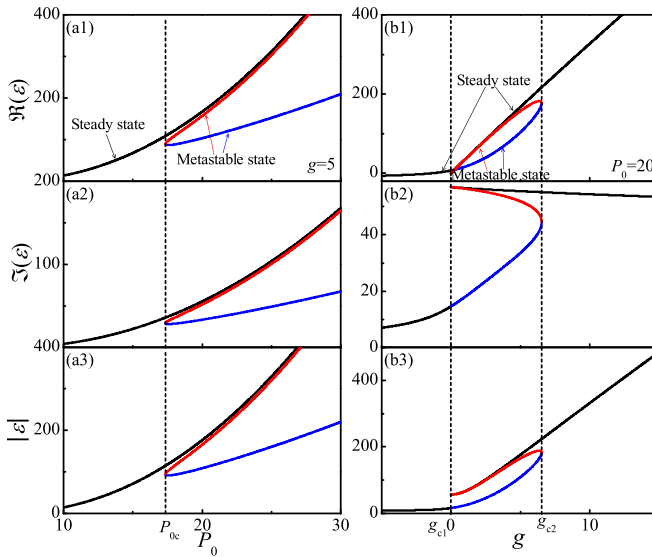
FIG. 2. Non-Hermitian spectrum of EPCs for different pumping power P_0 (a1)–(a3) and different polariton-polariton interaction g (b1)–(b3) with $\gamma = 5.0$, $\eta = 5.0$, and $w = 5.0$.

FIG. 3. Multistability of EPCs for $w = 5$. (a) EPC size $\bar{R}$ and particle number $\bar{n}$ in multistable states as a function of polariton-polariton interaction g for $P_0 = 20$, $\gamma = 5.0$, and $\eta = 5$ depicted by variational approach (solid lines) and numerical simulation of Eq. (1) (circles). (b) Phase trajectory in $R - n$ plane for different initial state with $g = 2.0$. (c) Temporal evolution of EPC size R and particle number n with $g = 2.0$ for different multistable states as marked A, B, and C in (a) and (b). (d) Multistability diagram in $P_0 - g$ plane with $\eta = 5$ (short dotted lines) and $\eta = 10$ (solid lines).

energies, where one is original spectral band corresponding to steady state (black lines), and the other two are emerging spectral bands corresponding to metastable states (red and blue lines). Therefore incoherent pumps can result in the spectrum bifurcation that induces the emergence of multistability.

However, when polariton-polariton interaction changes, there exist two exceptional points of non-Hermitian spectrum at $g = g_{c1}$ and $g = g_{c2}$ [Figs. 2(b1)–2(b3)]. For attractive ($g < g_{c1}$) and strong repulsive interactions ($g > g_{c2}$), the spectrum is degenerate, which corresponds to a steady state. For weak repulsive interactions ($g_{c1} < g < g_{c2}$), the spectrum bifurcation leads to the emergence of metastable states (red and blue lines). The spectral degeneracy of polariton condensates is different from the case in atomic condensates; it results from the non-Hermitian nature and is not caused by the nonlinearity as in traditional condensates. Therefore, control of related parameters allows us to manipulate the approach to non-Hermitian spectrum bifurcation and the generation of multistability for EPCs (see also Appendix B).

IV. MULTISTABILITY

The stability of multistable states can be explained by the corresponding dynamics. We introduce damping coefficient C_B for breathing dynamics and eigenvalues Λ for the characteristic matrix of linearizing dynamic evolution equations (Appendix D). Then positive C_B and negative $\text{Re}(\Lambda)$ can indicate the existence of long-lifetime EPCs.

When $g_{c1} < g < g_{c2}$, the multistability of EPCs appears and the system exhibits three equilibrium states: Two metastable states A and B and one steady state C [Fig. 3(a)]. For state A, $C_B < 0$ indicates that the oscillation amplitude of EPC size R is increasing with time, and $\text{Max}[\text{Re}(\Lambda)] > 0$ indicates that this state is unstable and cannot be maintained for a long lifetime [Fig. 4(a)]. The driven oscillation of EPC size leads to this state eventually evolving into steady-state C with a larger size [see Figs. 3(c), 4(c2), and 4(d2)]. State B is

maintained for a finite lifetime due to $C_B > 0$ and $\text{Max}[\text{Re}(\Lambda)] > 0$ [Fig. 4(a)]. For state C, $C_B > 0$ and $\text{Max}[\text{Re}(\Lambda)] < 0$ indicate that it can indeed exist for a long lifetime. In the region of multistability, regardless of the initial EPC size and particle number, the condensate will evolve into
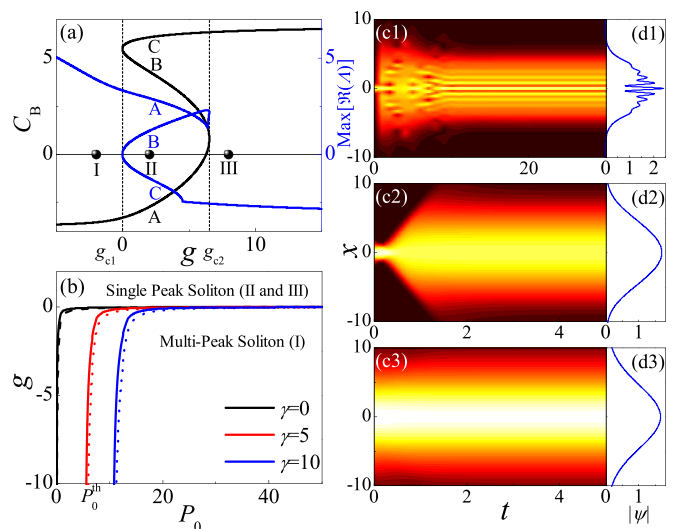
FIG. 4. Dynamics of EPCs with $w = 5.0$. (a) C_B and $\text{Max}[\text{Re}(\Lambda)]$ versus g with $P_0 = 20$, $\gamma = 5.0$ and $\eta = 5.0$. (b) The diagram for the single- and multipeak soliton in $P_0 - g$ plane with $\eta = 5.0$ (solid lines) and $\eta = 10.0$ (dotted lines). (c1)–(c3) The temporal evolution of EPCs depicted by numerical simulations of Eq. (1) for $g = -2.0$, 2.0, and 8.0 as marked by I, II, and III in (a). (d1)–(d3) The final spatial distribution for EPCs at $t = 50$ corresponding to (c1)–(c3).

steady-state C. It may pass by a metastable state A or B in the evolutionary process, which depends on the initial state [Fig. 3(b)]. These phenomena are induced by non-Hermitian skin effects. These states with a Gaussian distribution are also called single-peak solitons. This multistability is rooted in the non-Hermitian spectrum bifurcation.

The generation of multistability also depends on other parameters that can be obtained from the multistability diagram in Fig. 3(d). For strong enough pumping power P_0, multistability emerges in the region of $g_{c1} < g < g_{c2}$. Outside this region, the system only exhibits one steady state. With the enhancement of P_0, g_{c1} first increases quickly then tends to zero, while g_{c2} increases linearly. Therefore, an increasing in pumping power can enlarge the region of the multistability. On the other hand, the increased loss rate γ causes the multistable region to shift right, and the increased gain saturation η causes g_{c2} to shift up. Namely, the loss rate (the gain saturation) can shrink (enlarge) the region of multistability.

When $g > g_{c2}$, there is only one steady state with a single-peak soliton [Fig. 3(a)]. $C_B > 0$ and $\text{Max}[\text{Re}(\Lambda)] < 0$ indicate that the system can eventually evolve into a steady state for arbitrary perturbation due to the damping effect. The steady state can still be maintained as a single-peak soliton [Figs. 4(c3) and 4(d3)]. When $g < g_{c1}$, EPCs also exhibit one equilibrium state [Fig. 3(a)]. $C_B < 0$ and $\text{Max}[\text{Re}(\Lambda)] > 0$ indicate that this state is unstable [Fig. 4(a)]. The driven oscillation of EPC size leads to the breaking up of a single-peak soliton and eventually forming a multipeak soliton in Figs. 4(c1) and 4(d1) (for details, see Appendix E).

For a repulsive polariton-polariton interaction, steady states demonstrate as single-peak soliton structures. This soliton is called a dissipative soliton due to the driven-dissipative nature of EPCs. Steady states are important and possess potential applications compared with metastable states because steady states can be maintained for a long lifetime and are more stable.

For steady state with a single-peak soliton, solving dynamic evolution equations results in the number of exciton-polariton condensates

$$n(t) = \frac{\sqrt{2\pi}\bar{R}Gn_0}{\eta n_0 + (\sqrt{2\pi}\bar{R}G - \eta n_0)\exp(-Gt)}, \quad (3)$$

where n_0 is an initial polariton number, and $G = P_0 w/\sqrt{w^2 + \bar{R}^2} - \gamma$ is an effective net gain. It depends on the pumping power and size, loss rate, and EPC size. For homogeneous pumping (i.e., $w \to \infty$), the effective net gain $G = P_0 - \gamma$. Whatever the initial EPC number is, it can evolve into a saturated value $\bar{n} = \sqrt{2\pi}\bar{R}G/\eta$ which depends on effective net gain and saturation rate (Fig. 5). This phenomenon is rooted in the damping effects of nonequilibrium system in steady states (see also Appendix E).

EPC size and number in steady states are depicted in Fig. 6. Without polariton loss, the system is unstable because the EPC size is larger than the pumping size and EPCs will be diffused. However, considering the loss, the system is stable because EPC size is always smaller than pumping size when pumping powers increase (see also Appendix E). Furthermore, the polariton-polariton interaction g and pumping size
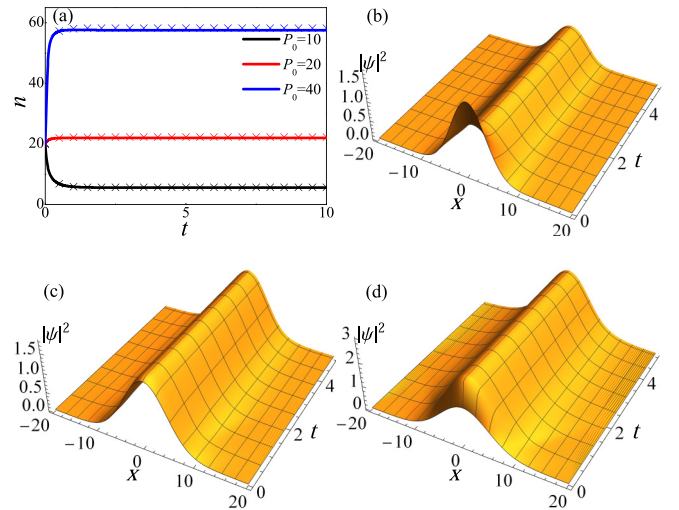
FIG. 5. Dissipative solitons for different pumping power P_0 with $g = \eta = \gamma = w = 5.0$. (a) Temporal evolutions for EPC number depicted by analytical expression Eq. (3) (solid lines) and numerical simulation of Eq. (1) (crosses). (b)–(d) The corresponding temporal evolution of solitons depicted by numerical simulation of Eq. (1) for $P_0 = 10$, 20, and 40, respectively.

w can increase the EPC number and size, while the loss rate γ and the gain saturation η can reduce them.

V. EXPERIMENTAL PROTOCOL

EPCs can be created in a semiconductor microwire and excited by a continuous nonresonant Gaussian pump beam as shown in Fig. 1. The nonresonant pump can be generated by a single mode Ti:sapphire laser [57], whose power and size can be controlled accurately. Polariton-polariton interactions
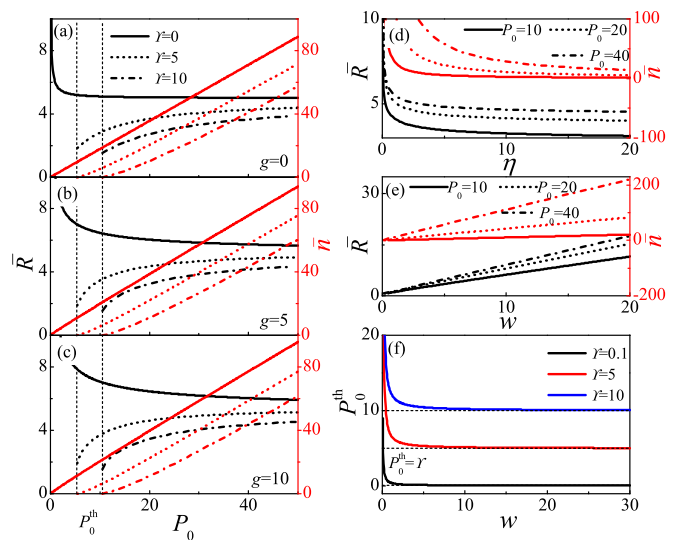
FIG. 6. Steady states for EPCs. (a)–(c) EPC size $\bar{R}$ and number $\bar{n}$ versus P_0 for different γ and g with $w = 5$ and $\eta = 5$. (d), (e) $\bar{R}$ and $\bar{n}$ versus η and g for different P_0 with $\gamma = g = 5$. (f) The critical pumping power for generating condensed polaritons P_0^{th} versus w for different γ.

can be adjusted from attractive to repulsive [66–68]. Loss rates can be controlled by adjusting the quality factor of microcavities [57]. The related parameters can be estimated by experiments [26,57]: $m \sim 5 \times 10^{-5} m_e$ with m_e being the free electron mass, $\omega \sim 0.01$ ps^{-1}, $l \sim 100\,\mu$m, $P_0 \sim 0.13$ meV/$(\hbar\omega)$, $w \sim l$, $\gamma \sim \omega$, $g \sim 7.9\,\mu$eVμm$^2/(\hbar\omega l^2)$, $\eta \sim g$. The non-Hermitian energy can be measured by analyzing the microcavity photoluminescence by means of energy resolved near-field (real-space) imaging using a spectrometer [56,59]. When coherent photons escape the cavity, the photoluminescence signal can carry all the information about the phase structure, density, spatial, momentum, and energy of EPCs [31]. Thus analyses of the photoluminescence enable us to depict spectrum about the energy vs real-space imaging, and the peak position and widths of the spectral lines correspond to the real and imaginary parts of the non-Hermitian energy, respectively [56] (see also Appendix B). Experimentally, non-Hermitian spectrum has been observed at the magnitude of meV (i.e., $10^3\hbar\omega$) [56]. Thus, our predicted non-Hermitian spectrum bifurcation and multistability can be easily realized with current experimental conditions.

VI. CONCLUSIONS

We have demonstrated the multistability of EPCs in the bifurcation region of the non-Hermitian spectrum. The spectrum provides a universal method for detecting transition from monostability to multistability. Multistability manifests itself in one steady and two metastable states, and the evolution from metastable to steady states induced by non-Hermitian skin effects can be used to design unidirectional switch [8–10]. We also discover a steady state with multipeak solitons in attractive EPCs, which is different from single-peak soliton in repulsive EPCs. The discovery could be useful in low-energy polariton-based devices exploiting optical multistability [6,7], which have fast switching times and could easily be realized at room temperature.

ACKNOWLEDGMENTS

APPENDIX A: VARIATIONAL ANALYSES

To obtain the steady-state solution and the dynamical evolution of the nonequilibrium system, we use the variational method for a dissipative system [64,65]. A nature variational ansatz is the Gaussian trial distribution. It is the well-known ground state of the conservative Bose-Einstein condensate.

Thus we take

$$\psi(x,t) = \left(\frac{n}{\sqrt{\pi}R}\right)^{1/2} \exp\left[-\frac{(x-\xi)^2}{2R^2} + ik(x-\xi) + \frac{i\delta}{2}(x-\xi)^2 + i\phi\right], \quad (A1)$$

which denotes that the polariton condensate has a Gaussian distribution with center mass position $\xi(t)$, momentum $k(t)$, size $R(t)$, the related variation rate of width $\delta(t)$, phase $\phi(t)$, and the number of condensed polaritons $n(t)$ (i.e., $n = \int |\psi|^2 dx$) at a given time t. Inserting Eq. (A1) into the Euler-Lagrangian equations for dissipative system,

$$\frac{\partial L}{\partial q_i} - \frac{d}{dt}\left(\frac{\partial L}{\partial \dot{q}_i}\right) = 2\text{Re}\left[\int_{-\infty}^{+\infty} \frac{i}{2}(P - \gamma - \eta|\psi|^2)\psi\frac{\partial \psi^*}{\partial q_i}\right], \quad (A2)$$

where $q_i = \{\xi, k, R, \delta, n, \phi\}$ and the Lagrangian corresponds to the conservative system

$$L = \int \frac{1}{2}\left[i(\psi^*\dot{\psi} - \dot{\psi}^*\psi) - \left(\left|\frac{\partial \psi}{\partial x}\right|^2 + g|\psi|^4\right)\right]dx, \quad (A3)$$

we arrive at

$$\dot{\xi} = k - P_0 E R^2 w\xi, \quad (A4)$$

$$\dot{k} = -P_0 E R^2 w\delta\xi, \quad (A5)$$

$$\dot{R} = R\delta + \frac{\eta n}{4\sqrt{2\pi}} - \frac{1}{2}P_0 E R^3 w + \frac{P_0 E R^3 w\xi^2}{w^2 + R^2}, \quad (A6)$$

$$\dot{\delta} = -\delta^2 + \frac{1}{R^4} + \frac{gn}{\sqrt{2\pi}R^3}, \quad (A7)$$

$$\dot{n} = \left[P_0 E w(w^2 + R^2) - \gamma - \frac{\eta n}{\sqrt{2\pi}R}\right]n, \quad (A8)$$

where $E = \exp[-\xi^2/(w^2 + R^2)](w^2 + R^2)^{-3/2}$. Once the evolution behavior of variational parameters $q_i(t)$ is acquired from Eqs. (A4)–(A8), the nonequilibrium dynamics of polariton condensate can be described clearly. The revelent steady state (i.e., $q_i(t) \equiv \bar{q}_i$) can also be obtained by the corresponding stationary equations of Eqs. (A4)–(A8). Obviously the width of condensed polariton R depends on its number n and center position ξ, and there are coupled effects among dipolar dynamics, breathing dynamics, and particle flux.

In the equilibrium state, we have $\bar{\xi} = 0$ and $\bar{k} = 0$, and

$$\bar{\delta} + \frac{\eta\bar{n}}{4\sqrt{2\pi}\bar{R}} - \frac{P_0 w\bar{R}^2}{2(w^2 + \bar{R}^2)^{3/2}} = 0, \quad (A9)$$

$$\bar{\delta}^2 - \frac{1}{\bar{R}^4} - \frac{g\bar{n}}{\sqrt{2\pi}\bar{R}^3} = 0, \quad (A10)$$

$$\left[\frac{P_0 w}{\sqrt{w^2 + \bar{R}^2}} - \gamma - \frac{\eta\bar{n}}{\sqrt{2\pi}\bar{R}}\right]\bar{n} = 0. \quad (A11)$$

Namely, the particle number and size of condensed polaritons can be obtained by Eqs. (A9)–(A11) in the equilibrium state.
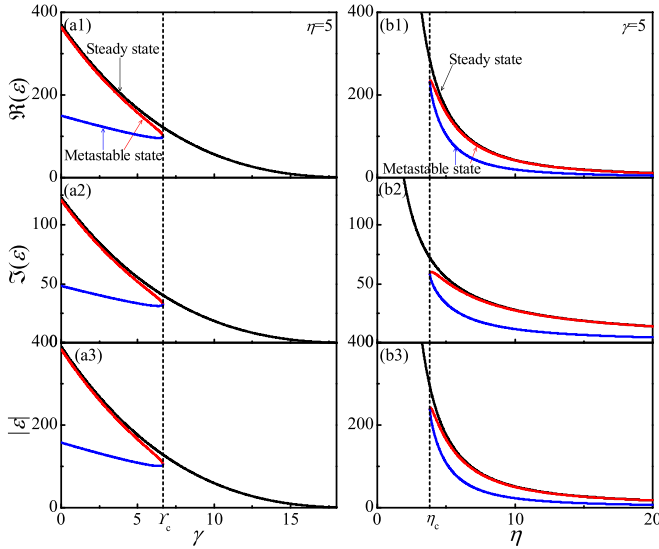
FIG. 7. Non-Hermitian spectrum of exciton-polariton condensates for different loss rate γ (a1)–(a3) and different gain saturation η (b1)–(b3) with $P_0 = 20.0$, $g = 5.0$, and $w = 5.0$. Black solid lines correspond to steady state, while red and blue solid lines correspond to metastable states.

The non-Hermitian eigenenergies of polariton condensates can be obtained by the following equation:

$$\varepsilon = \int dx \left\{ \frac{1}{2} |\nabla \psi|^2 + \frac{g}{2} |\psi|^4 + \frac{i}{2} \left[P(x) |\psi|^2 - \gamma |\psi|^2 + \frac{1}{2} \eta |\psi|^4 \right] \right\}. \quad (A12)$$

Inserting Eq. (A1) into Eq. (A12), we can obtain the real part of non-Hermitian eigenenergies

$$\mathrm{Re}(\varepsilon) = \frac{1}{2} nk^2 + \frac{n}{4R^2} + \frac{1}{4} nR^2 \delta^2 + \frac{gn^2}{2\sqrt{2\pi}R}, \quad (A13)$$

and the imaginary part

$$\Im(\varepsilon) = \frac{P_0 wn \exp\left(-\frac{\xi^2}{w^2+R^2}\right)}{2\sqrt{w^2+R^2}} - \frac{1}{2} \gamma n - \frac{\eta n^2}{4\sqrt{2\pi}R}. \quad (A14)$$

APPENDIX B: SUPPLEMENTAL NON-HERMITIAN SPECTRUM

Here the spectrum reveals the dependence of the energy in different steady states on system parameters even though the energy is a complex number. In a polariton condensate, there is indeed a collective frequency related to an oscillating macroscopic photon field. This frequency depends on the rate of interconversion between excitons and photons [59]. However, this frequency can be regarded as a constant for distinct multistable states, and the corresponding energy can be omitted in the spectrum. As supplementary, Fig. 7 demonstrates the non-Hermitian spectrum of exciton-polariton condensates for a different loss rate and gain saturation. There is one exceptional point in the non-Hermitian spectrum for a varying loss rate at $\gamma = \gamma_c$ as shown in Figs. 7(a1)–7(a3). For a small loss rate, i.e., $\gamma < \gamma_c$, there are three spectrum bands.

They correspond to three equilibrium states: One steady state (black lines) and two metastable states (red and blue lines). For a large loss rate, i.e., $\gamma > \gamma_c$, there is only one spectrum band which corresponds to the steady state, and the other two bands corresponding to metastable states appear. Therefore the increase of loss rate can move the system away from the non-Hermitian spectrum bifurcation to degeneracy through an exceptional point. It results in the disappearance of multistability.

Non-Hermitian spectrum in a codimension 2 space (i.e., $g - P_0$ space) is depicted in Fig. 8. As pumping power P_0 increases, there is an exceptional point of spectrum P_{0c}. When $P_0 < P_{0c}$, the spectrum is degenerate, and when $P_0 > P_{0c}$, the spectrum is bifurcated. As polariton-polariton interactions increase, there are two exceptional points of spectrum g_{c1} and g_{c2}; the spectrum is degenerate for $g < g_{c1}$ and $g > g_{c2}$, while the spectrum is bifurcated for $g_{c1} < g < g_{c2}$. Thus, exceptional points exactly connect to spectrum degeneracy and bifurcation.

Physical quantities (such as the exciton-polariton condensate size R, related variation rate of width δ, and number n) describing the character of condensates are continuous variables and not quantized. Thus the corresponding energy is also a continuous variable, and the spectrum is a continuous curve.

Exceptional points are also transition points from monostability to multistability, which connect to monostable states and multistable states. A multistable state contains one steady and two metastable states. Namely, an exceptional point simultaneously connects with one steady state and two metastable states. Thus exceptional points connecting with the steady state and the metastable state are same.

The effect of the gain saturation on the non-Hermitian spectrum is demonstrated in Figs. 7(b1)–7(b3). The gain saturation can move the system away from the non-Hermitian spectrum degeneracy to bifurcation through an exceptional point. It results in the appearance of multistability. The loss rate and gain saturation can both decrease the real part and the imaginary part of energies. The region of spectrum bifurcation (i.e., the region of the multistability) is shown in Fig. 3(d). The loss rate and repulsive polariton-polariton interaction can shrink (enlarge) the region of the multistability. The pumping power and gain saturation can enlarge the region of the multistability.

Non-Hermitian spectrum bifurcation and the appearance of multistability are also related to pumping size, which is demonstrated in Fig. 9. There is a critical pumping size w_c for generating multistability (i.e., non-Hermitian spectrum exceptional point). When pumping size $w < w_c$, the spectrum is degenerate and the system is monostable. When $w > w_c$, the spectrum is bifurcate and multistability appears. In the region of monostability, the spectrum is degenerate, and in the region of multistability, the spectrum is bifurcated. In the spectrum, the energy degeneracy and bifurcation are connected by an exceptional point. Thus this transition point is exactly the exceptional point of spectrum. In a word, increasing pumping size moves the system away from the non-Hermitian spectrum degeneracy toward bifurcation, which induces a transition from monostability to multistability.

The spectrum cannot be directly measured in experiments because the non-Hermitian energy is a complex number.
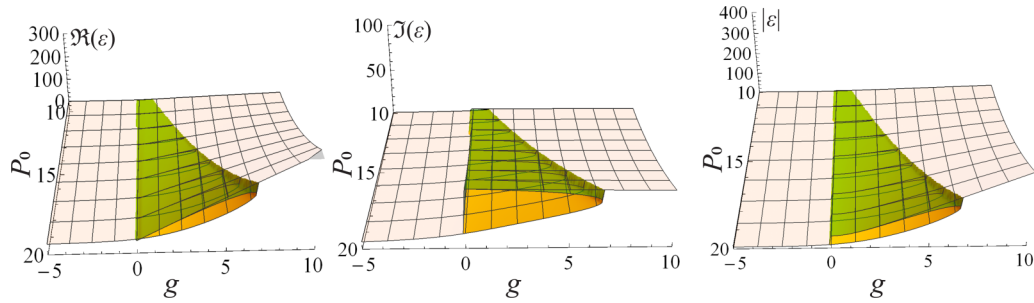
FIG. 8. Non-Hermitian spectrum of exciton-polariton condensates in the $g - P_0$ space with $w = 5.0$, $\gamma = 5.0$, and $\eta = 5.0$. The spectrum is continuous, and exceptional points are the transition point between monostability and multistability.

However, we can measure the real part and the imaginary part of the non-Hermitian energy, respectively. The shape of exciton-polariton condensates can be directly imaged both in real and in momentum space. The real part of non-Hermitian energy can be measured by energy resolved images of the polaritons using a spectrometer [59]. The imaginary part of non-Hermitian energy results from the finite polariton lifetime, and it can be measured by detecting the escaping light from the cavity [59]. Actually, the non-Hermitian energy has already been measured in the experiment of Ref. [56]. The non-Hermitian energy is obtained by analysis of the microcavity photoluminescence by means of energy resolved near-field (real-space) imaging, where the real part corresponds to the energy peak position and the imaginary part corresponds to the line width.

In order to observe our predicted non-Hermitian spectrum bifurcation and multistability experimentally, exciton-polariton condensates can be created in a quasi-onedimensional semiconductor microwire and excited by a continuous nonresonant Gaussian pump beam as shown in Fig. 1. The semiconductor microcavity device is comprised of QWs placed between two distributed Bragg reflectors. The QWs are located at the antinodes of the photon mode. Generally, QWs are GaAs thin layers with the order of 10nm thickness, and distributed Bragg reflectors consist of multiple pairs of alternated AlAs and GaAs layers. Exciton-polariton condensates have typical lifetime on the order of 100ps and condensation temperature on the order of 10K in GaAs and CdTe semiconductors [35,36,56].

Due to the continuous decay of the exciton polaritons in the continuous replenished condensed state, coherent photons escape the cavity as a photoluminescence signal and carry all the information about the spatial, momentum, phase structure, and energy of the condensed exciton polaritons [31]. The photoluminescence can be collected via a free space microscope and analyzed with a combination of real space and dispersion imaging techniques. Then, the energy vs real-space imaging can be presented, and the peak position and widths of the spectral lines correspond to the real and imaginary parts of the non-Hermitian energy, respectively. Experimentally, non-Hermitian spectrum has observed at the magnitude of meV (i.e., $10^3 \hbar\omega$) [56]. Thus, our predicted non-Hermitian spectrum of exciton-polariton condensates can be easily observed with current experimental conditions.

APPENDIX C: SELF-LOCALIZATION

In order to understand the dipolar dynamics of the system, we assume $R \equiv \bar{R}$, $\delta \equiv \bar{\delta}$, and $n \equiv \bar{n}$. Thus the dipolar dynamics can be described by the following equation:

$$\ddot{\xi} + C_D \dot{\xi} + \Omega_D^2 \xi = 0, \qquad (C1)$$

where $C_D = P_0 w \bar{R}^2 \bar{E}[1 - 2\xi^2/(w^2 + \bar{R}^2)]$ and $\Omega_D^2 = P_0 w \bar{R}^2 \bar{\delta}$ with $\bar{E} = \exp[-\xi^2/(w^2 + \bar{R}^2)](w^2 + \bar{R}^2)^{-3/2}$. In the multistable state, $\xi = \bar{\xi} = 0$ and nonzero center mass position $\pm\bar{\xi}$ do not exist [see Eqs. (A4)–(A5)]. This is induced by Gaussian pump $P(x) = P_0 \exp(-x^2/w^2)$ that is centered at $x = 0$. Thus, whatever initial center mass position ξ_0 is, we have $\xi^2 < (w^2 + \bar{R}^2)/2$ for some ξ, i.e., $C_D > 0$. This results in the damping dipolar dynamics, and the center mass position of exciton-polariton condensates eventually approach to zero. Namely, the Gaussian pump leads to the self-localization of exciton-polariton condensates. This has been observed in experiment [57]. The temporal evolutions of the related soliton for the damping dipolar dynamics are
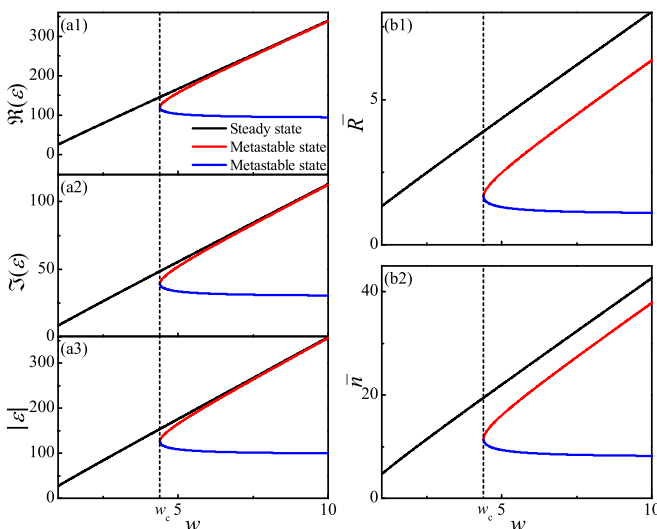
FIG. 9. Non-Hermitian spectrum and multistability of exciton-polariton condensates depending on pumping size w with $P_0 = 20.0$, $g = 5.0$, $\gamma = 5.0$, and $\eta = 5.0$. (a1)–(a3): Non-Hermitian spectrum for different w. (b1)–(b2): Exciton-polariton condensate size $\bar{R}$ and particle number $\bar{n}$ in multistable states as a function of w. Black solid lines correspond to steady state, while red and blue solid lines correspond to metastable states.
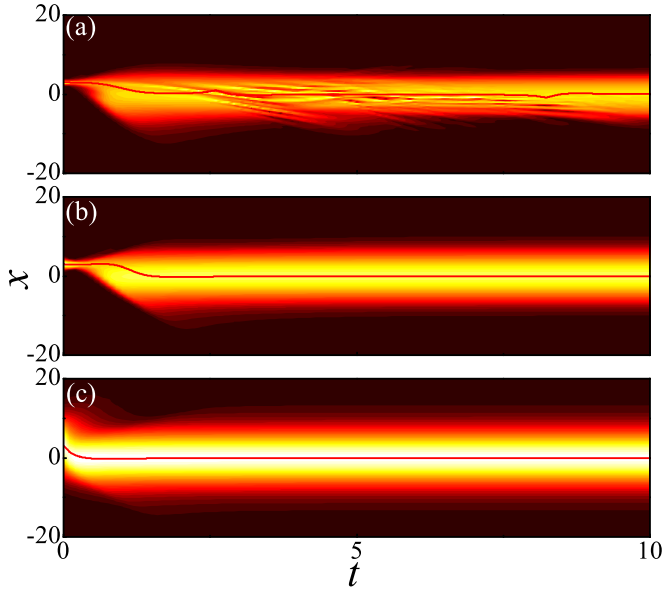
FIG. 10. The damping dipolar dynamics for initial center mass position $\xi_0 = 3.0$ with $w = 5.0$, $\gamma = 5.0$, $\eta = 5.0$, and $g = -2.0$, 2.0, and 8.0 [(a)–(c)]. The temporal evolution of the exciton-polariton condensates (the contour plot) is depicted by the directly numerical simulation of open-dissipative Gross-Pitaevskii equation and the the mass center position ξ (red lines) is depicted by the variational analysis Eqs. (A4)–(A8).

demonstrated in Fig. 10 for different steady state regions, which agrees with the variational predictions.

APPENDIX D: STABILITY ANALYSES

The stability of multistable states can be explained by the corresponding dynamics of exciton-polariton condensates. Near the multistable state, we have $\xi \equiv 0$, then from Eqs. (A6)–(A8) the breathing dynamics can be obtained by the following equation:

$$\ddot{R} + C_B \dot{R} + \Omega_B^2 R = 0, \tag{D1}$$

where $C_B = 0.5 P_0 w R^2 (4w^2 + R^2)(w^2 + R^2)^{-5/2} - \eta n/(4\sqrt{2\pi}R)$, and $\Omega_B^2 = \eta\gamma n/(4\sqrt{2\pi}R) - 1/R^4 - gn/(\sqrt{2\pi}R^3) + 5\eta^2 n^2/(32\pi R^2) + P_0^2 w^2 R^4/(4(w^2 + R^2)^3) - P_0 w\eta n(w^2 + 2R^2)/(4\sqrt{2\pi}(w^2 + R^2)^{3/2}R)$. If $C_B < 0$, the breathing dynamics is driven and the oscillation amplitude of polariton size R is always increasing, then the system is unstable. If $C_B > 0$, the breathing dynamics is damped and the oscillation amplitude of R decreases and eventually tends to a fixed size $\bar{R}$, then the system is stable. Furthermore, the stability of system can also be discussed by linearizing Eqs. (A6)–(A8) around the multistable state. Inserting $q_i = \bar{q}_i + q_i'$ into Eqs. (A6)–(A8), we have

$$\frac{d}{dt}\begin{pmatrix} n' \\ R' \\ \delta' \end{pmatrix} = \mathbf{M}\begin{pmatrix} n' \\ R' \\ \delta' \end{pmatrix}, \tag{D2}$$

where,

$$\mathbf{M} = \begin{pmatrix} \frac{P_0 w}{w^2 + \sqrt{\bar{R}^2}} - \frac{2\eta\bar{n}}{\sqrt{2\pi}\bar{R}} - \gamma & \frac{\eta\bar{n}^2}{\sqrt{2\pi}\bar{R}^2} - \frac{P_0 w\bar{R}\bar{n}}{(w^2 + \bar{R}^2)^{3/2}} & 0 \\ \frac{\eta}{4\sqrt{2\pi}} & \bar{\delta} - \frac{3P_0 w^3\bar{R}^2}{2(w^2 + \bar{R}^2)^{5/2}} & \bar{R} \\ \frac{g}{\sqrt{2\pi}\bar{R}^3} & -\frac{3\bar{n}}{\sqrt{2\pi}\bar{R}^4} - \frac{4}{\bar{R}^5} & -2\bar{\delta} \end{pmatrix}. \tag{D3}$$

The stability can be obtained by the eigenvalue Λ of the matrix $\mathbf{M}$. If the real parts of the eigenvalues $\mathrm{Re}(\Lambda)$ are all negative, the corresponding equilibrium state is stable, and can be maintained for long lifetime. If $\mathrm{Re}(\Lambda)$ is a positive value, the corresponding multistable state is unstable, and its lifetime is short.

APPENDIX E: MULTI- AND SINGLE-PEAK SOLITONS

Here, multipeak solitons is only demonstrated by direct numerical simulation of Eq. (1) and cannot be obtained by variational analyses with trial wave function Eq. (2). The boundary between the single- and multipeak soliton is demonstrated in Fig. 5(b). For $P_0 > P_0^{th}$, g_{c1} divides the diagram of steady states into two, one is the multipeak soliton region ($g < g_{c1}$) and the other is the single-peak soliton region ($g > g_{c1}$). As P_0 increases, g_{c1} increases quickly and then approaches a constant that is less than zero. Thus the generation of multipeak soliton is induced by attractive polariton-polariton interaction. The loss rate and gain saturation can both shrink the region of multipeak solitons. The mechanism for generating multipeak solitons in exciton-polariton condensates is expounded, i.e., the strong polariton-polariton attractive interaction leads to the breaking up of single-peak soliton and eventually forming a multipeak soliton. These multipeak solitons can be maintained for a long time as shown in Fig. 4(d1). This phenomenon leads to the deviation between variational analyses and numerical results in attractive interaction regions as shown in Fig. 3(a).

These spatially modulated multipeak solitons play a significant role in the information transmission. However, here we focus on non-Hermitian spectrum and the transition between monostability and multistability while explaining this transition throng exceptional points of spectrum. Therefore, regarding multipeak solitons, we only demonstrate their existence in the region of attractive interaction and reveal the formation mechanism.

In the region of repulsive polariton-polariton interactions, steady states demonstrate as solitonlike structures. This soliton is called as dissipative soliton due to the driven-dissipative nature of exciton-polariton condensates. Steady states are important and possess potential applications compared with metastable states, because steady states can be maintained for a long lifetime and are more stable.

In order to more clearly understand the property of exciton-polariton condensates in steady states, we perturb the polariton number near the steady state and depict the temporal evolution of the corresponding dissipative solitons and exciton-polariton condensate number in Fig. 5. When exciton-polariton condensates are supersaturated initially, i.e., $n_0 > \bar{n}$, where $\bar{n} = \sqrt{2\pi}\bar{R}G/\eta$ is the exciton-polariton condensate number in the steady state (also called the saturated state),

it dissipates until $n_0 = \bar{n}$ [see Figs. 5(a) and 5(b)]. When exciton-polariton condensates do not reach to saturation, i.e., $n_0 < \bar{n}$, the exciton-polariton condensate number quickly increases to $\bar{n}$ [see Figs. 5(a) and 5(d)]. When exciton-polariton condensates are saturated, i.e., $n_0 = \bar{n}$, the exciton-polariton number still remains unchanged [see Figs. 5(a) and 5(c)]. Hence, whatever the initial exciton-polariton condensate number is, it can evolve to a saturated value $\bar{n}$ which depends on effective net gain and saturation rate. These results are good agreement with predictions of Eq. (3). This phenomenon is rooted in the damping effects of a nonequilibrium system in steady states.

The size and particle number of exciton-polariton condensates in the steady state is clearly depicted in Fig. 6. As shown in Fig. 6(a), without polariton loss (i.e., $\gamma = 0$), the increase of pumping power leads to the exciton-polariton condensate size that first quickly decreases then remains

unchanged and the exciton-polariton condensate number always increases. In this case, the system is unstable because the exciton-polariton condensate size is larger than the pumping size and they will be diffuse. However, when considering the loss (i.e., $\gamma \neq 0$) and $P_0 > P_0^{\text{th}}$, the exciton-polariton condensate size first quickly increases then tends to a constant and the exciton-polariton condensate number increases as pumping power enhances. When $P_0 \leqslant P_0^{\text{th}}$, there is no condensed polariton, i.e., $\bar{n} = 0$. Furthermore, the polariton-polariton interaction g and pumping size w can increase the exciton-polariton condensate number and size while the loss rate γ and the gain saturation η can decrease them. The critical pumping power threshold for generating condensed polariton $P_0^{\text{th}} = \sqrt{\gamma/2}(1 + \sqrt{1 + 2\gamma w^2}/w)$ is reduced by the pumping size and promoted by the loss rate, which is depicted in Fig. 6(f).

[1] A. Baas, J. Ph. Karr, H. Eleuch, and E. Giacobino, Phys. Rev. A **69**, 023809 (2004).

[2] Y. Dong, J. W. Ye, and H. Pu, Phys. Rev. A **83**, 031608(R) (2011).

[3] P. Treutlein, D. Hunger, S. Camerer, T. W. Hänsch, and J. Reichel, Phys. Rev. Lett. **99**, 140403 (2007).

[4] W. Fujita and K. Awaga, Science **286**, 261 (1999).

[5] R. W. Boyd, *Nonlinear Optics* (Academic Press, San Diego, 2003).

[6] M. Sich, F. Fras, J. K. Chana, M. S. Skolnick, D. N. Krizhanovskii, A. V. Gorbach, R. Hartley, D. V. Skryabin, S. S. Gavrilov, E. A. Cerda-Méndez, K. Biermann, R. Hey, and P. V. Santos, Phys. Rev. Lett. **112**, 046403 (2014).

[7] H. S. Nguyen, D. Vishnevsky, C. Sturm, D. Tanese, D. Solnyshkov, E. Galopin, A. Lemaitre, I. Sagnes, A. Amo, G. Malpuech, and J. Bloch, Phys. Rev. Lett. **110**, 236601 (2013).

[8] M. De Giorgi, D. Ballarini, E. Cancellieri, F. M. Marchetti, M. H. Szymanska, C. Tejedor, R. Cingolani, E. Giacobino, A. Bramati, G. Gigli, and D. Sanvitto, Phys. Rev. Lett. **109**, 266407 (2012).

[9] A. V. Uvarov, S. S. Gavrilov, V. D. Kulakovskii, and N. A. Gippius, Phys. Rev. A **99**, 033837 (2019).

[10] A. Dreismann, H. Ohadi, Y. del V. I. Redondo, R. Balili, Y. G. Rubo, S. I. Tsintzos, G. Deligeorgis, Z. Hatzopoulos, P. G. Savvidis, and J. J. Baumberg, Nat. Mater. **15**, 1074 (2016).

[11] T. Tanabe, M. Notomi, S. Mitsugi, A. Shinya, and E. Kuramochi, Opt. Lett. **30**, 2575 (2005).

[12] L. Pickup, K. Kalinin, A. Askitopoulos, Z. Hatzopoulos, P. G. Savvidis, N. G. Berloff, and P. G. Lagoudakis, Phys. Rev. Lett. **120**, 225301 (2018).

[13] M. Amthor, T. C. H. Liew, C. Metzger, S. Brodbeck, L. Worschech, M. Kamp, I. A. Shelykh, A. V. Kavokin, C. Schneider, and S. Höfling, Phys. Rev. B **91**, 081404(R) (2015).

[14] D. Bajoni, E. Semenova, A. Lemaître, S. Bouchoule, E. Wertz, P. Senellart, S. Barbay, R. Kuszelewicz, and J. Bloch, Phys. Rev. Lett. **101**, 266402 (2008).

[15] D. Ballarini, M. De Giorgi, E. Cancellieri, R. Houdré, E. Giacobino, R. Cingolani, A. Bramati, G. Gigli, and D. Sanvitto, Nat. Commun. **4**, 1778 (2013).

[16] O. Kyriienko, T. C. H. Liew, and I. A. Shelykh, Phys. Rev. Lett. **112**, 076402 (2014).

[17] Y. V. Kartashov, V. V. Konotop, and L. Torner, Phys. Rev. B **86**, 205313 (2012).

[18] S. I. Tsintzos, N. T. Pelekanos, G. Konstantinidis, Z. Hatzopoulos, and P. G. Savvidis, Nature (London) **453**, 372 (2008).

[19] B. Deveaud-Plédran, Nature (London) **453**, 297 (2008).

[20] X. K. Ma and S. Schumacher, Phys. Rev. Lett. **121**, 227404 (2018).

[21] N. A. Gippius, I. A. Shelykh, D. D. Solnyshkov, S. S. Gavrilov, Y. G. Rubo, A. V. Kavokin, S. G. Tikhodeev, and G. Malpuech, Phys. Rev. Lett. **98**, 236401 (2007).

[22] T. K. Paraïso, M. Wouters, Y. Léger, F. Mourier-Genoud, and B. Deveaud-Plédran, Nat. Mater. **9**, 655 (2008).

[23] C. Ouellet-Plamondon, G. Sallen, F. Morier-Genoud, D. Y. Oberli, M. T. Portella-Oberli, and B. Deveaud, Phys. Rev. B **93**, 085313 (2016).

[24] E. Z. Tan, H. Sigurdsson, and T. C. H. Liew, Phys. Rev. B **97**, 075305 (2018).

[25] H. Sigurdsson, I. A. Shelykh, and T. C. H. Liew, Phys. Rev. B **92**, 195409 (2015).

[26] J. Kasprzak, M. Richard, S. Kundermann, A. Baas, P. Jeambrun, J. M. J. Keeling, F. M. Marchetti, M. H. Szymańska, R. André, J. L. Staehli, V. Savona, P. B. Littlewood, B. Deveaud, and L. S. Dang, Nature (London) **443**, 409 (2006).

[27] S. Christopoulos, G. Baldassarri Höger von Högersthal, A. J. D. Grundy, P. G. Lagoudakis, A. V. Kavokin, J. J. Baumberg, G. Christmann, R. Butté, E. Feltin, J. F. Carlin, and N. Grandjean, Phys. Rev. Lett. **98**, 126405 (2007).

[28] J. J. Baumberg, A. V. Kavokin, S. Christopoulos, A. J. D. Grundy, R. Butté, G. Christmann, D. D. Solnyshkov, G. Malpuech, G. Baldassarri, H. von Högersthal, E. Feltin, J. F. Carlin, and N. Grandjean, Phys. Rev. Lett. **101**, 136409 (2008).

[29] J. D. Plumhof, T. Stöferle, L. Mai, U. Scherf, and R. F. Mahrt, Nature Mater. **13**, 247 (2014).

[30] R. Su, S. Ghosh, J. Wang, S. Liu, C. Diederichs, T. C. H. Liew, and Q. Xiong, Nat. Phys. **16**, 301 (2020).

[31] H. Deng, H. Haug, and Y. Yamamoto, Rev. Mod. Phys. **82**, 1489 (2010).

[32] I. Carusotto and C. Ciuti, Rev. Mod. Phys. **85**, 299 (2013).

[33] T. Byrnes, N. Y. Kim, and Y. Yamamoto, Nat. Phys. **10**, 803 (2014).

[34] C. E. Whittaker, E. Cancellieri, P. M. Walker, D. R. Gulevich, H. Schomerus, D. Vaitiekus, B. Royall, D. M. Whittaker, E. Clarke, I. V. Iorsh, I. A. Shelykh, M. S. Skolnick, and D. N. Krizhanovskii, Phys. Rev. Lett. **120**, 097401 (2018).

[35] T. Gao, E. Estrecho, K. Bliokh, T. Liew, M. Fraser, S. Brodbeck, M. Kamp, C. Schneider, S. Höfling, Y. Yamamoto, F. Nori, Y. S. Kivshar, A. G. Truscott, R. G. Dall, and E. A. Ostrovskaya, Nature (London) **526**, 554 (2015).

[36] M. Pieczarka, E. Estrecho, M. Boozarjmehr, O. Bleu, M. Steger, K. West, L. N. Pfeiffer, D. W. Snoke, J. Levinsen, M. M. Parish, A. G. Truscott, and E. A. Ostrovskaya, Nat. Commun. **11**, 429 (2020).

[37] D. Sanvitto and V. Timofeev, eds., *Exciton Polaritons in Microcavities*, *New Frontiers, Springer Series in Solid-State Sciences* (Springer, New York, 2012), Vol. 172.

[38] M. Wouters, T. K. Paraïso, Y. Léger, R. Cerna, F. Morier-Genoud, M. T. Portella-Oberli, and B. Deveaud-Plédran, Phys. Rev. B **87**, 045303 (2013).

[39] V. Goblot, B. Rauer, F. Vicentini, A. Le Boité, E. Galopin, A. Lemaître, L. Le Gratiet, A. Harouri, I. Sagnes, S. Ravets, C. Ciuti, A. Amo, and J. Bloch, Phys. Rev. Lett. **123**, 113901 (2019).

[40] H. Hu and X. J. Liu, Phys. Rev. A **101**, 011602(R) (2020).

[41] L. Salasnich, B. A. Malomed, and F. Toigo, Phys. Rev. E **90**, 043202 (2014).

[42] X. R. Xu, Y. Hu, Z. D. Zhang, and Z. X. Liang, Phys. Rev. B **96**, 144511 (2017).

[43] T. M. Wang, Z. P. Li, Z. G. Lu, Y. M. Li, S. N. Miao, Z. Lian, Y. Z. Meng, M. Blei, T. Taniguchi, K. Watanabe, S. Tongay, W. Yao, D. Smirnov, C. W. Zhang, and S. F. Shi, Phys. Rev. X **10**, 021024 (2020).

[44] G. Roumpos, M. D. Fraser, A. Löffler, S. Höfling, A. Forchel, and Y. Yamamoto, Nat. Phys. **7**, 129 (2011).

[45] L. Zhang, W. Xie, J. Wanga, A. Poddubny, J. Lu, Y. Wang, J. Gu, W. Liu, D. Xu, X. Shen, Y. G. Rubo, B. L. Altshuler, A. V. Kavokin, and Z. Chen, Proc. Natl. Acad. Sci. USA **112**, E1516 (2015).

[46] F. Baboux, L. Ge, T. Jacqmin, M. Biondi, E. Galopin, A. Lemaître, L. Le Gratiet, I. Sagnes, S. Schmidt, H. E. Türeci, A. Amo, and J. Bloch, Phys. Rev. Lett. **116**, 066402 (2016).

[47] M. V Berry, Ann. Phys. **131**, 163 (1981).

[48] T. Guhr, A. Müller-Groeling, and H. A. Weidenmüller, Phys. Rep. **299**, 189 (1998).

[49] K. Y. Bliokh, Y. P. Bliokh, V. Freilikher, A. Z. Genack, and P. Sebbah, Phys. Rev. Lett. **101**, 133901 (2008).

[50] C. W. Zhang, J. Liu, M. G. Raizen, and Q. Niu, Phys. Rev. Lett. **93**, 074101 (2004).

[51] M. V. Berry, Czech. J. Phys. **54**, 1039 (2004).

[52] W. D. Heiss, J. Phys. A **45**, 444016 (2012).

[53] R. Hanai, A. Edelman, Y. Ohashi, and P. B. Littlewood, Phys. Rev. Lett. **122**, 185301 (2019).

[54] C. E. Rüter, K. G. Makris, R. El-Ganainy, D. N. Christodoulides, M. Segev, and D. Kip, Nat. Phys. **6**, 192 (2010).

[55] B. Peng, Ş. K. Özdemir, S. Rotter, H. Yilmaz, M. Liertzer, F. Monifi, C. M. Bender, F. Nori, and L. Yang, Science **346**, 328 (2014).

[56] T. Gao, G. Li, E. Estrecho, T. C. H. Liew, D. Comber-Todd, A. Nalitov, M. Steger, K. West, L. Pfeiffer, D. W. Snoke, A. V. Kavokin, A. G. Truscott, and E. A. Ostrovskaya, Phys. Rev. Lett. **120**, 065301 (2018).

[57] D. Ballarini, I. Chestnov, D. Caputo, M. De Giorgi, L. Dominici, K. West, L. N. Pfeiffer, G. Gigli, A. Kavokin, and D. Sanvitto, Phys. Rev. Lett. **123**, 047401 (2019).

[58] J. Keeling and N. G. Berloff, Phys. Rev. Lett. **100**, 250401 (2008).

[59] J. Keeling and N. G. Berloff, Contemp. Phys. **52**, 131 (2011).

[60] M. Wouters and I. Carusotto, Phys. Rev. Lett. **99**, 140402 (2007).

[61] Z. X. Liang, Z. D. Zhang, and W. M. Liu, Phys. Rev. Lett. **94**, 050402 (2005).

[62] C. Y. Jia, R. K. Wu, Y. Hu, W. M. Liu, and Z. X. Liang, arXiv:1907.13300.

[63] F. I. Moxley, J. P. Dowling, W. Dai, and T. Byrnes, Phys. Rev. A **93**, 053603 (2016).

[64] Y. Xue and M. Matuszewski, Phys. Rev. Lett. **112**, 216401 (2014).

[65] A. Ankiewicz, N. Akhmediev, and N. Devine, Opt. Fiber Tech. **13**, 91 (2007).

[66] L. Dominici, M. Petrov, M. Matuszewski, D. Ballarini, M. De Giorgi, D. Colas, E. Cancellieri, B. Silva Fernández, A. Bramati, G. Gigli, A. Kavokin, F. Laussy, and D. Sanvitto, Nat. Commun. **6**, 8993 (2015).

[67] E. Estrecho, T. Gao, N. Bobrovska, D. Comber-Todd, M. D. Fraser, M. Steger, K. West, L. N. Pfeiffer, J. Levinsen, M. M. Parish, T. C. H. Liew, M. Matuszewski, D. W. Snoke, A. G. Truscott, and E. A. Ostrovskaya, Phys. Rev. B **100**, 035306 (2019).

[68] L. B. Tan, O. Cotlet, A. Bergschneider, R. Schmidt, P. Back, Y. Shimazaki, M. Kroner, and A. İmamoğlu, Phys. Rev. X **10**, 021011 (2020).